Elucidating the Localized Plasmonic Enhancement Effects from a Single Ag Nanowire in Organic Solar Cells

Xinfeng Liu,[†,‖] Bo Wu,[†,‡,‖] Qing Zhang,[†] Jing Ngei Yip,[†] Guannan Yu,[†] Qihua Xiong,[†,§] Nripan Mathews,[*,‡,⊥] and Tze Chien Sum[*,†]

[†]Division of Physics and Applied Physics, School of Physical and Mathematical Sciences, Nanyang Technological University, 21 Nanyang Link, Singapore 637371, Singapore, [‡]Energy Research Institute @ NTU (ERI@N), 1 CleanTech Loop, #06-04 CleanTech One, Singapore 637141, Singapore, [§]NOVITAS, Nanoelectronics Center of Excellence, School of Electrical and Electronic Engineering, Nanyang Technological University, Singapore 639798, Singapore, and [⊥]Division of Materials Technology, School of Materials Science and Engineering, Nanyang Technological University, Block N4.1 Nanyang Avenue, Singapore 639798, Singapore. [‖]These authors (X.L. and B.W.) contributed equally to this work.

ABSTRACT The origins of performance enhancement in hybrid plasmonic organic photovoltaic devices are often embroiled in a complex interaction of light scattering, localized surface plasmon resonances, exciton—plasmon energy transfer and even nonplasmonic effects. To clearly deconvolve the plasmonic contributions from a single nanostructure, we herein investigate the influence of a single silver nanowire (NW) on the charge carriers in bulk heterojunction polymer solar cells using spatially resolved optical spectroscopy, and correlate to electrical device characterization. Polarization-dependent photocurrent enhancements with a maximum of ~36% over the reference are observed when the transverse mode of the plasmonic excitations in the Ag NW is activated. The ensuing higher absorbance and light scattering induced by the electronic motion perpendicular to the NW long axis lead to increased exciton and polaron densities instead of direct surface plasmon-exciton energy transfer. Finite-difference time-domain simulations also validate these findings. Importantly, our study at the single nanostructure level explores the fundamental limits of plasmonic enhancement achievable in organic solar cells with a single plasmonic nanostructure.

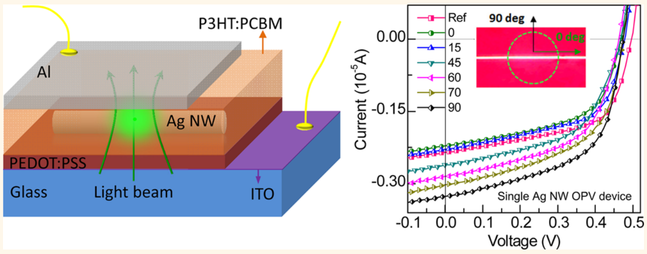

KEYWORDS: organic solar cells · plasmonic · silver nanowire · single nanostructure · spatially resolved spectroscopy · performance improvement

Bulk heterojunction (BHJ) organic solar cells (OSCs) possess attractive properties for applications as lightweight, flexible and large area solar energy harvesting devices.[1−5] Although the power conversion efficiencies (PCEs) of these cells have exceeded 9%,[6−8] a major bottleneck hampering its efficiency improvement is the compromise between the absorption of photons and extraction of charges that limits the thickness of the active layer. A promising solution is to leverage on plasmonic nanostructures to achieve optically thick yet physically thin layers.[9−14] Such plasmonic effects manifest through (a) subwavelength scattering to increase the optical path length, (b) near-field focusing that increases electron—hole pair generation, or (c) excitation of localized surface plasmon polaritons at the metal-dielectric interface.[15] These metal nanostructures are typically embedded either in the charge transport layer or in the active BHJ layer.[15−23] Presently, most works focus on the macroscopic optical and electrical properties of hybrid plasmonic organic photovoltaic (OPV) devices. Although device performance improvements following metallic nanostructure incorporation are frequently reported and attributed to plasmonic effects,[22−25] such improvements could also arise from nonplasmonic origins: *e.g.*, reduction of bulk resistance due to improved conductivity of the metal nanoparticles,[22] or augmented hole extraction due to the enlarged interfacial area by metal nanostructures.[26] Consequently, it is unclear how much enhancement is truly plasmonic in nature.[27−33] Few works have directly examined the plasmonic enhancement realistically

* Address correspondence to
Tzechien@ntu.edu.sg,
Nripan@ntu.edu.sg.

Received for review May 25, 2014
and accepted September 8, 2014.

Published online September 08, 2014
10.1021/nn505020e

© 2014 American Chemical Society

achievable from a single nanostructure in plasmonic organic solar cells.

Ultrafast optical spectroscopy (UOS) techniques are powerful tools for probing carrier and quasi-particle dynamics, capable of tracing their lifetimes from generation to recombination.[34] Correlating their kinetics with device performance metrics yields valuable insights into the origins of the plasmonic enhancements or detraction in plasmonic OPV devices. Characterizing the individual behavior of a single metal nanostructure using these techniques will circumvent any ensemble average effects and allow us to examine the limits of plasmonic enhancements in an OPV environment. Herein, the surface plasmon effects of a single silver nanowire (Ag NW) on the performance of poly(3-hexythiophene) (P3HT) and [6,6]-phenyl-C61-butyic acid methyl ester (PCBM) solar cells were investigated using spatially resolved transient absorption and time-resolved photoluminescence spectroscopy together with spatially resolved electrical measurements. The quasi-one-dimensional (1-D) Ag NWs present an intriguing model system to investigate the polarization dependent plasmonic effects, which would otherwise be absent in symmetrical systems like metallic microspheres.[35−38] Toward these objectives, we still have to rationalize that we are indeed observing true plasmonic effects that enhances OPV performance when Ag NW is added. Thus, this may give an impression that we are conflating between the works of single particle experiments with those that explore whether addition of small plasmonic nanostructures enhances solar cell performance.[27−30] However, the focus of our work remains on elucidating the localized plasmonic enhancement effects from a single Ag NW in organic solar cells. A maximum enhancement of ∼36% in short circuit current density is obtained when the transverse mode plasmonic excitation perpendicular to the NW long axis is activated. Finite-difference time-domain (FDTD) simulations validate that the efficiency improvement is mainly from the larger absorption and light scattering caused by the localized surface plasmon instead of direct surface plasmon-exciton energy transfer.

RESULTS AND DISCUSSION

Figure 1a shows a schematic of the plasmonic OPV device structure, where Ag NWs are used as the plasmonic elements. The Ag NWs are located near the PEDOT:PSS and P3HT:PCBM interface with approximately half of the NW embedded in either layer for effective light scattering (see later FDTD simulation results).[34] The as-prepared Ag NWs are capped by ligands of PVP, which are reported to be effective in eliminating the charge/energy transfer losses between organic materials and metallic structures.[39] Scanning electron microscope (SEM) images in Figure 1b show that these Ag NWs have a relatively uniform diameter of around 60 nm and a length of several micrometers. Figure 1c shows the optical micrographs of a single Ag NW in bright field (top), dark field (middle) and the corresponding SEM image (bottom). The 60 nm diameter NWs used for the study is a compromise between using smaller sized NWs, which have weaker light scattering and a larger surface-to-volume ratio that can lead to more surface traps, and using larger diameter NWs that will cause undesirable effects of strong metal absorption losses, shadowing effects, upsetting the BHJ morphology and shunting issues, *etc.*[40] Here, a small amount of Ag NWs (0.06 g/mL) is used in our films and devices. It was found to have minimal effects on the surface morphology resolvable by AFM (AFM images, see Supporting Information Figure S1), though we cannot rule out changes in molecular-scale morphology in the films surrounding the nanowires as have been found by other authors.[41]

The optical properties of a single Ag nanowire were investigated using a home-built confocal microscopy setup (see Supporting Information Figure S2 for the details). Polarization dependence from a single bare Ag NW on a quartz substrate is evident from both the absorption spectra (see Figure 1d) and scattering spectra (see Figure 1e). Here, the angles are defined with respect to the long axis of the Ag NW with 0° as the light polarization along the long axis and 90° as the light polarization perpendicular to the long axis. The resonance peak at ∼420 nm (90°) corresponds to the transverse mode of the plasmonic excitations in the single Ag NW, yielding the localized surface plasmon resonance (LSPR) peak.[42−44] For the peak located at around 540 nm, it is unlikely to be the longitudinal mode as such mode is known from the literature to be located in the infrared for 1D Ag nanowire of length >200 nm.[45] Using FDTD simulations (see Supporting Information Figures S3 and S4), we establish that this 540 nm peak originates from the scattering and is likely a propagation mode that is related to the surface plasmon polaritons (SPPs) in the silver nanowire. In Figure 1f, higher absorbance of the unpolarized white light in the presence of a single Ag NW is observed from the absorption spectra of P3HT:PCBM. This is ascribed to the increased light absorption in the active P3HT:PCBM layer from the excited localized SPPs at the metal/dielectric interfaces and from the scattering effects around Ag NW.[18,46]

To elucidate the effects of an individual Ag NW to the OPV device, we examine the generation and recombination kinetics of the P3HT excitons, first for the bare P3HT films and then the P3HT:PCBM blends. Spatially resolved PL and TRPL measurements were conducted on Ag/P3HT samples. Figure 2a shows that the PL intensity gradually increases as the incident polarization was tuned from 0 to 90° with respect to the NW axis. For angles between 0 and 20°, the PL intensity from the NW sample is weaker than the control

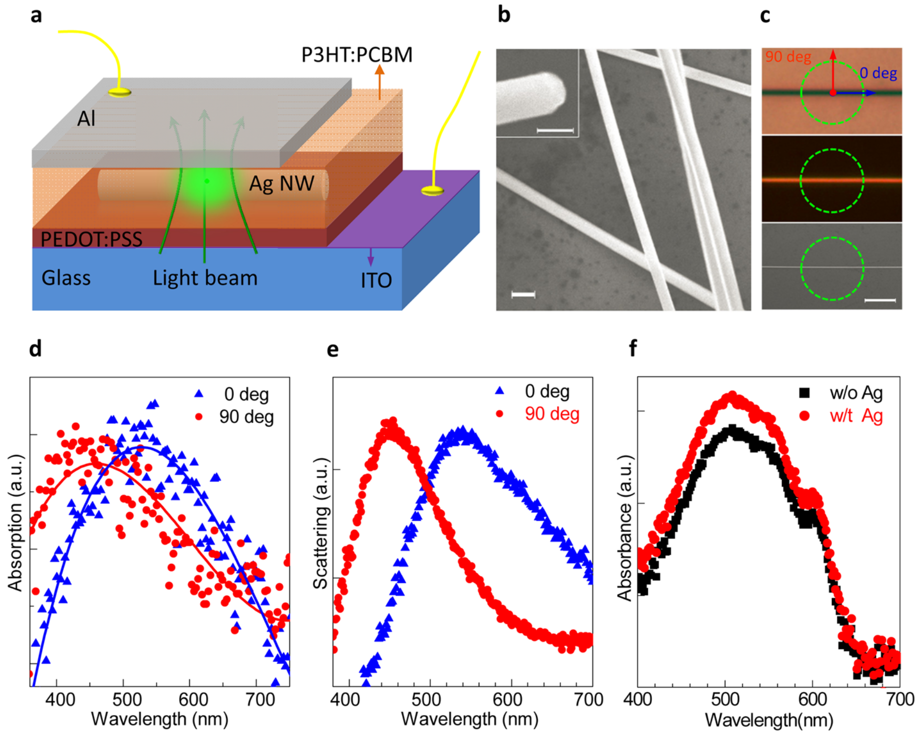

Figure 1. Single Ag NW characterization in an OPV device geometry. (a) Representative illustration of the OPV device geometry with a single Ag NW embedded in the PEDOT:PSS layer. (b) SEM images of Ag NWs, scale bar 100 nm, (inset) magnified SEM image of a typical Ag NW with diameter ∼60 nm, where the scale bar is 50 nm. (c) From top to bottom, optical image (transparent mode), optical image (dark field mode), and the corresponding SEM image of a single Ag NW. The dotted green circle is the approximate area where the optical signals are collected. The polarization of incident light is defined as perpendicular (90° of polarization) and parallel (0° of polarization) to the long axis of the Ag NW. Polarization dependent absorption spectra (d), scattering spectra (e), for the single Ag NW (on quartz) collected from the area defined in (c). (f) Absorption spectra of P3HT:PCBM with and without Ag NW, measured using an unpolarized white light (spot size ∼2 μm in diameter) in an optical microscope.

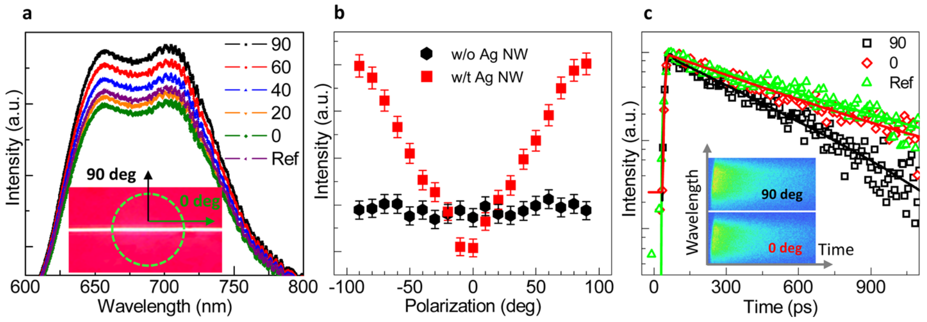

Figure 2. Polarization dependent PL and TRPL spectra of P3HT film with single Ag NW. (a) PL of the P3HT film with a single Ag NW following excitation with different polarization of light. Inset is an optical micrograph of the single NW where the pump polarization is perpendicular (90° of polarization) and parallel (0° of polarization) to the long axis of the Ag NW. The dotted green circle is the approximate area where the optical signals are collected. (b) Polarization dependence of the PL intensity for P3HT film with a single Ag NW. (c) The PL decay dynamics of P3HT excitons with and without Ag NW following laser excitation with different polarizations. Inset are typical streak camera images of the PL decay for P3HT film with a single Ag NW following excitation by 0 and 90° polarized laser beams.

(the control spectrum was measured on close regions without Ag NW). At angles larger than 20°, the PL intensity increases continuously and surpasses that of the control (see Figure 2b). The P3HT light absorption and emission is strongly affected by the presence of the Ag NW as expected. At 0° (light polarization along the Ag NW long axis), there is some shadowing effect from the Ag NW (∼several μm long which is much larger than the wavelength of light). Therefore, light absorption by P3HT is decreased. At 90° polarization, the NW diameter is several tens of nanometers, which is much smaller compared to the incident wavelength. The redistribution of the local electric fields leads to an enhanced absorption of P3HT, thereby increasing the exciton density which in turn results in higher PL intensity.

Figure 2c shows the PL recombination dynamics after photoexcitation by 400 nm femtosecond laser

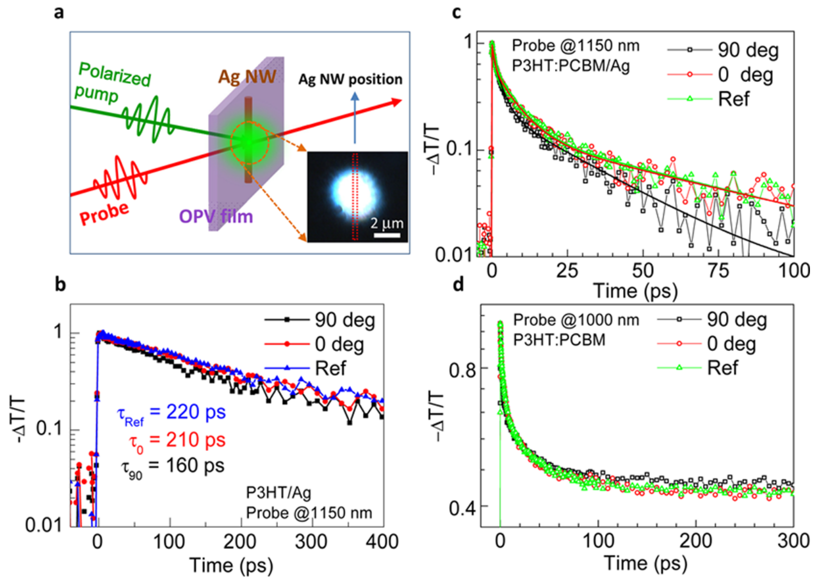

Figure 3. Microtransient absorption spectroscopy on single Ag NW OPV film. (a) Schematic of the microtransient absorption (μ-TA) measurement on a single Ag NW embedded OPV film: the image shows the overlapped pump and probe beams. Inset shows an optical micrograph of the laser spot and the red dotted outline indicates the approximate location of the Ag NW. (b) Photoinduced absorption (PIA) decay dynamics of the singlet excitons monitored at 1150 nm for reference P3HT-only film and that with a single Ag NW for different polarized pump excitations. (c) PIA decay dynamics of the singlet excitons monitored at 1150 nm for reference P3HT:PCBM film and that with a single Ag NW for different polarized pump excitations. (d) PIA decay dynamics of the polarons (overlapped with those from the excitons) monitored at 1000 nm for reference P3HT:PCBM film and that with a single Ag NW for different polarized pump excitations.

pulses, with the pump fluence kept to a low of ~2 μJ cm^{-2} to minimize any higher order effects. The dynamics over the spectral region of 650−720 nm can be well-fitted using a single exponential decay function, indicating the presence of only one emissive photoexcited species (*i.e.*, the singlet exciton). The lifetime for the control P3HT film is 560 ± 10 ps, which is also independent of the polarization of incident light. For 0° polarization (along the NW long axis) in the P3HT sample with Ag NW, the fits yield a lifetime of 473 ± 8 ps, which decreased to 314 ± 5 ps for 90° polarization. This small change in exciton lifetime (by ~33%) indicates that the interaction between the P3HT excitons and the transverse LSPR modes in the NW is in the weak coupling regime.[41,47] Such couplings between the plasmons and excitons would lead to an increased exciton recombination rate.[18,22,48] In the previous work by Oo and colleagues,[24] the random orientation of the Au NWs and the ensemble-averaged TRPL measurements would smear out and preclude any such distinctions in their lifetimes.

To probe the exciton dynamics of the P3HT:PCBM blends in the vicinity of a single Ag NW, PL lifetime measurements are not feasible due to the strong quenching of the P3HT emission in the blends. A complementary approach using spatially resolved or microscopic transient absorption (μ-TA) was performed instead. Figure 3a shows a schematic of the μ-TA measurement over the locality of the Ag NW (see Supporting Information Figure S5 for the setup). We first monitored the decay profile at around 1150 nm (from singlet exciton recombination; see later discussion) for P3HT films as shown in Figure 3b. A lifetime of ~220 ± 10 ps was observed for P3HT films, which is in quantitative agreement with the lifetime (~560 ± 10 ps) observed by TRPL measurements on P3HT films although slightly smaller. However, fluorescence dynamics may not be representative of the exciton dynamics because the excitons undergo nonradiative decay. Transient absorption spectroscopy, which is more sensitive to the total exciton population, would be more suitable to assess the dynamics of the excitons.[49] For P3HT film with silver nanowire, the lifetimes at 0 and 90° were 210 ± 10 and 160 ± 10 ps, respectively. The lifetime shortening at 90° excitation is also consistent with the PL lifetime shortening as shown in Figure 2c.

Figure 3c,d show the photoinduced absorption (PIA) dynamics (or $-\Delta T/T$) of the P3HT:PCBM transient spectra[49,50] at the probe wavelengths of 1150 and 1000 nm. From previous literature,[50,51] the PIA peak at 1150 nm was assigned as the singlet excitons, while the peak around 1000 nm was attributed to the overlapping signatures from P3HT polarons in disordered domains, P3HT singlet excitons, and PCBM anions. Two lifetimes are obtained from the fits of the singlet excitons decay dynamics (Figure 3c), with the shorter lifetime arising from the charge transfer of excitons generated close to the donor/acceptor (D/A) interface while the longer lifetime is assigned to the quenching of the excitons following diffusion to the D/A interface.[50] These lifetimes for P3HT:PCBM reference and for that with the single Ag NW (at 0 and 90° polarizations) are listed in Table 1. The near invariance of the singlet lifetimes for 0 and 90° polarizations (with Ag NW) and that of the reference suggest the lack of any strong interactions between the P3HT excitons and the LSPR modes. This observation indicates that the fast quenching of the excitons at the donor–acceptor interface has affected the exciton–plasmon coupling observed in the earlier TRPL measurements of the Ag NW/P3HT only films. It should be mentioned that the transient absorption spectra for Ag NW/P3HT film (see Figure 3c) also suggests the interaction between the P3HT excitons and the transverse LSPR modes (*i.e.*, 90° excitation) in the Ag NW. This result is consistent with the TRPL results shown in Figure 2c.

From Figure 3c, we can see that the singlet exciton decay is almost completed within the first 100 ps. However, for the 1000 nm peak (Figure 3d), the long-lived nonzero background indicates the existence of a long lifetime (up to microseconds, not shown here). This long lifetime is ascribed to the polaron decay. It can also be seen that the contribution from polarons is slightly larger with 90° polarization light excitation than that of 0°. It indicates that more polarons are generated with 90° polarization light excitation, suggesting that the localized plasmonic effect possibly enhance exciton dissociation to polarons, albeit not so efficiently. Correlating the spatially resolved TRPL and μ-TA measurements, it is clear that the presence of the Ag NW increases the population of the excitons and carriers, but has little effect on the charge separation processes.

TABLE 1. Fitted Parameters for the PIA decay of the Singlet Excitons at 1150 nm for the P3HT:PCBM Sample without Ag NW (Reference) and That with Ag NW (at 0 or 90° Excitation)

	A_1	τ_1(ps)	A_2	τ_1(ps)
Reference	0.29 ± 0.01	1.8 ± 0.1	0.19 ± 0.01	19 ± 1
0 deg	0.29 ± 0.01	1.6 ± 0.1	0.20 ± 0.01	19 ± 1
90 deg	0.33 ± 0.01	1.9 ± 0.1	0.15 ± 0.01	20 ± 1

To examine the localized effects of a Ag NW in an OPV device configuration, we conducted *I*–*V* studies at the specific device regions with and without a single Ag NW. For spatially resolved selective excitation of the specific localized regions, we used a 532 nm CW laser as the excitation source instead of a white light source because chromatic aberrations from the latter would result in the focusing of different wavelengths at different depths. The 532 nm wavelength is also close to the LSPR peak located around 550 nm (see Figure 5c inset). The excitation fluence used here is ~3.2 W/cm^2, which is one order larger than that of a solar simulator with an average intensity of ~0.1 W/cm^2. However, at much lower pump fluence (*i.e.*, ~0.1 W/cm^2), the signal-to-noise is poor. Therefore, the higher fluence used here is a compromise. From the curves shown in Figure 4a, the best electrical performance was obtained when the incident light polarization is perpendicular to the NW long axis, with an enhancement of the short circuit current density J_{sc} by ~36% compared to a similarly sized reference area without Ag NW. Single Ag NW measurements of other devices are also given in Supporting Information Figure S6 where the maximum enhancement ranges between 26 and 32%. When the incident pump light polarization is parallel to the Ag NW direction, the relative J_{sc} drops by ~6% as compared to the reference area. Note that the fill factor (FF) for all these cases is relatively poor compared to typical values found in the literature. This is due to the much higher illumination intensity used here that causes more bimolecular recombination losses, thereby reducing the FF.[52] Figure 4b shows the polarization dependence of the J_{sc} values. Such polarization dependence hints that the collected charges (originating from exciton and polaron generation) is boosted by the transverse LSPR mode

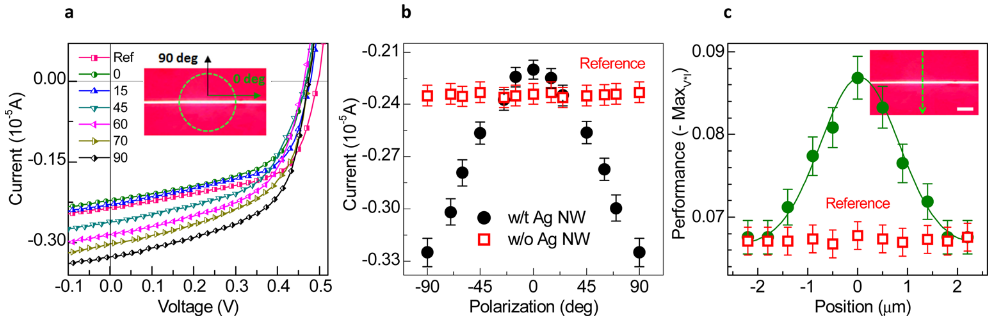

Figure 4. Polarization dependent micro/localized *I*–*V* characterization of a single Ag NW device. (a) Microarea *I*–*V* curves with different polarizations of the pump laser. Inset is an optical micrograph of the single NW where the pump polarization is perpendicular (90° of polarization) and parallel (0° of polarization) to the long axis of the Ag NW. The dotted green circle is the approximate area where the optical signals are collected. (b) Polarization dependence of the short circuit current J_{sc} for the reference and single Ag NW region: data extracted from Figure 2a. (c) Localized device performance when perpendicularly polarized light is scanned across the single Ag NW. The definition of localized performance is expressed as the Maximum of $I \times V$ from the *I*–*V* curve. Left inset shows an optical micrograph of the single silver nanowire (white horizontal line). The vertical green dashed arrow is the scanning direction and the scale bar is 1 μm.

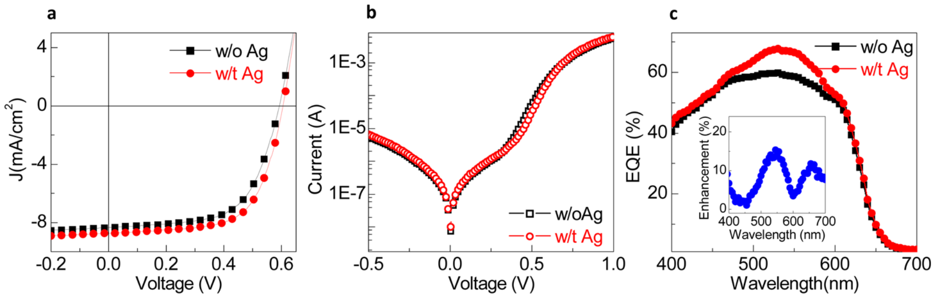

Figure 5. Full device (macro-area) *I*−*V* curves for OPV devices with and without Ag NWs. Representative *I*−*V* curve of the OPV device with and without Ag NWs under (a) illumination and (b) dark condition. (c) EQE data for the reference and plasmonic device. Inset shows the relative EQE enhancement.

TABLE 2. Device Performances of the Reference and Plasmonic Devices

	PCE (%)	J_{sc} (mA cm^{-2})	V_{oc} (V)	FF	R_s (Ωcm^2)	R_{sh} (kΩcm^2)
Reference	3.06 ± 0.12	−8.36 ± 0.22	0.59 ± 0.01	0.59 ± 0.01	3.72	26.4
Plasmonic devices	3.40 ± 0.10	−8.74 ± 0.18	0.60 ± 0.01	0.60 ± 0.01	3.60	23.1
Best Plasmonic devices	3.59	−9.01	0.61	0.61	3.75	58.0

in the NW. Lastly, by keeping the light polarization fixed (*i.e.*, transverse to the NW long axis) and scanning the laser spot over the NW along a pathway perpendicular to the NW long axis (see Figure 4c), an optimal localized *I*−*V* value is obtained when there is maximum coverage of the Ag NW by the laser spot (*i.e.*, at the zero position), further validating the role of the Ag NW. The enhanced localized device performance value over the reference also clearly shows that performance is not adversely affected by the shadowing effects from the Ag NW itself with perpendicularly polarized light.

To assess the reliability of the single Ag NW doped OPV *I*−*V* studies, full device (macro-area) electrical characterization is necessary for gauging the overall device performance improvements. Here, functional devices with and without Ag NWs were characterized under illumination with a solar simulator. In Figure 5a, the current density−voltage (*J*−*V*) characteristics of the control and hybrid plasmonic devices were shown. The device performance increased from 3.1 ± 0.1% (reference) to 3.4 ± 0.1% (with Ag NWs), from an average of 10 cells each as shown in Table 2. The performance of the best hybrid plasmonic device is ~3.59%, which is consistent with efficiency enhancements reported for such systems; see Supporting Information Table S1 for a comparison with similar plasmonic OPV systems reported in the literature.[10,16,18,53] The major contribution to this improvement is ascribed to the short-circuit current density (J_{sc}) increase from 8.36 to 8.74 mA cm^{-2} although the FF also undergo slight amelioration from 0.62 to 0.64. For the best performing hybrid plasmonic device with Ag NWs, its J_{sc} and FF could reach 9.01 mA cm^{-2} and 0.66, respectively. Dark *I*−*V* characteristics in Figure 5b indicate that both the shunt and series resistances are comparable for the control and hybrid devices. Although it may be possible that the plasmonic device performance may be further optimized by increasing the loading of Ag NWs, it is a balance between this and the undesirable changes to the film morphology, which would result in large variations in their performances. Nonetheless, the focus of our work here is to obtain clear analysis of the plasmonic effects; therefore, optimization of the Ag NWs loading was not performed. Figure 5c gives the external quantum efficiency (EQE) plots for the plasmonic and the reference devices. The EQE enhancement (inset of Figure 5c) occurs over the 500−600 nm regions with a maximum at ~550 nm. This enhancement clearly points to a LSPR origin with the enhancement peak red-shifted by ~100 nm compared to the LSPR peak of Ag NW ~420 nm (Figure 1e), where the Ag NW was on a quartz substrate and the measurement was in air.[54,55] It is reasonable since the dielectric environment in the plasmonic device is much higher (*i.e.*, P3HT:PCBM refractive index $n \sim 2.1$ in the visible range) which will lead to a significant redshift of LSPR according to Mie theory.[56]

Lastly, FDTD simulations were also carried out to have a better understanding of the field distribution by the single Ag NW. The simulations show that the Ag NW focuses and redistributes the incident light to the active P3HT:PCBM layer when the incident polarization is perpendicular to the NW direction (*i.e.*, 90°, TM) (Figure 6a). Such local field enhancements in P3HT:PCBM are beneficial for exciton and polaron generation. However, if the incident polarization is along the NW direction (*i.e.*, 0°, TE) (Figure 6b), light penetration to the active layer would be blocked and the scattering is mainly focused in the ITO layer. For comparison, the *E* field distribution for the control (without Ag NW) is also shown in Figure 6c. It is evident that the distribution of the electric field in the active layer is uniform and relatively weak compared to that in Figure 6a.

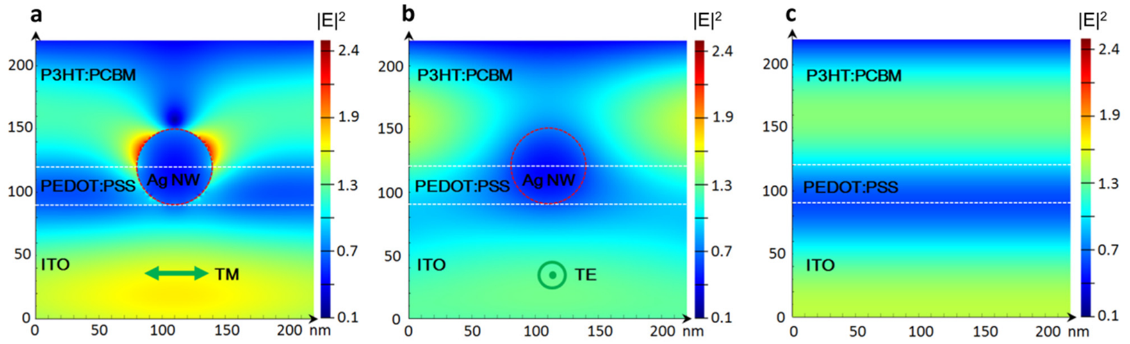

Figure 6. Electric field distribution in single Ag NW OPV device. Electric field distribution in the plasmonic device when the incident light (532 nm) is polarized (a) perpendicular (90° of polarization) and (b) parallel (0° of polarization) to the long axis of the Ag NW. (c) *E* field distribution in the reference device without Ag NW.

CONCLUSION

In summary, this study down to the single plasmonic nanostructure level using time-resolved microscopic techniques clearly reveals the complex interplay of photophysical effects (*i.e.*, polarization, excitonic and plasmonic) and structural effects influencing the performance of plasmonic solar cells. Our findings would help clarify some of the perplexing results in the literature. The large J_{sc} enhancement by ~36% for a single nanostructure indicates that there is still room for improvement for plasmonic OPV devices. Careful design, fabrication, passivation and placement of the metal nanostructures is essential to ensure that the desired polarization dependent surface plasmon modes are activated to ensure optimal light scattering to the active layers. Combing these findings from kinetic studies with electrical characterization is of paramount importance for careful data interpretation. With judicious control of these structure–function relations, plasmonic OPV remains a viable approach for further efficiency improvements to OPV devices.

METHODS

Ag NW Synthesis and Characterization. Ag NWs were synthesized through a slow titration method reported in the previous literature.[35,57,58] Typical synthesis begins with a mixture of 0.668 g of polyvinylpropyline (PVP) and 0.022 g of KBr in 20 mL of ethylene glycol which is heated to 170 °C for 20–30 min. The silver seeds are then introduced to the solution by adding 0.050 g of silver chloride (AgCl) into the solution and then followed by a slow titration of the growth solution, 0.22 g silver nitrate ($AgNO_3$) in 10 mL of ethylene glycol, for 12–15 min. The titration of the $AgNO_3$ progressively stacks Ag^+ ions onto the silver seeds, while the PVP restricts this stacking to anisotropic growth of one-dimensional NW, and the KBr salt precursor moderates the wire diameter to ensure long thin NWs. The solution remains at 170 °C for 30 additional minutes to complete the NW growth. The dispersion is then centrifuged three times with methanol at 6000 rpm for 30 min each time to extract the NWs from the dispersion. The final precipitate was dried and redispersed in 20 mL of methanol for further use. The diameter of Ag NWs was determined by a scanning electron microscope (SEM, JEOL 7001F).

Device Preparation and Electrical Characterization. Indium tin oxide (ITO) glass was cleaned using a standard procedure described previously.[34] Silver NWs in methanol solution were then dispersed onto ITO substrate by spin-coating at 1000 rpm. Thirty nanometer PEDOT:PSS was then spin-coated as hole transporting layer. The substrates were transferred to an inert environment and baked at 120 °C for 5 min. After that, P3HT:PCBM (weight ratio 1:0.8) was spin-coated to get a 100 nm thick film. Device fabrication was accomplished by evaporating a 100 nm thick Al cathode above the active layer and annealing at 150 °C for 20 min. For macroscopic characterization, control cells without Ag NWs were also fabricated. Effective area of each cell was 0.071 cm^2. For macroscopic measurements, $I-V$ characteristics of the devices under illumination and in the dark were measured with a HP 4155 semiconductor analyzer. Device performance was recorded using Air Mass 1.5 Global (AM 1.5 G) solar simulator (San-Ei XES-300, AAA rating) with an irradiation intensity of 0.1 W m^{-2} and averaged over 5–10 cells. The IPCE spectra were measured using a Merlin radiometry system with a build-in 150 W Newport-Oriel xenon lamp as light source. The light source was spectral resolved with Cornerstone monochromator. A Hamamatsu silicon photodiode was used as the reference. All the film depositions and device characterizations were done in inert environment. For microscopy measurements, devices were sealed using epoxy and a piece of cover glass. Keithley 2420 source meter was used to record $I-V$ curves. The cell was illuminated using a 532 nm green laser diode module with pump power of 0.1 μw (this power is measured just after microscope objective). Reference measurement was done by light shining the adjacent regions without any Ag NWs.

Optical Measurement. Microscopic nondegenerate femtosecond transient absorption spectroscopy (μ-TAS) was performed. The 500 nm pump pulses were tuned from an optical parametric amplifier (Light Conversion TOPAS) that was pumped by a 1-kHz regenerative amplifier (Coherent Legend; 800 nm; 150 fs; 1 mJ per pulse), which was in turn seeded by an 80 MHz Coherent Vitesse oscillator. A white light continuum probe spanning 450–1200 nm was generated using a sapphire plate. The collinear pump and probe beams were focused onto the sample using a microscope objective. Then the probe signal was coupled out by another objective. Pump-induced changes to the probe transmittance were measured using a monochromator/PMT configuration (visible light) and IR-monochromator/InGaAs photodetector configuration (NIR light). To mitigate the effects of higher order recombination, the excitation intensity was kept to a minimal of ~20 μJ cm^{-2}. The pump fluences used here are likely to induce higher-order effects, and as a result care should be taken when comparing the kinetics directly to device data. Femtosecond TAS can be measured with a spectral range 520–1200 nm and a temporal range from 0 ps to 2 ns to probe the carrier dynamics in organic solar cells. Time-resolved photoluminescence (TRPL) measurements were performed using excitation pulses from a Mira 900 fs laser system with output wavelength 800 nm and a repetition rate of 76 MHz. Typically, the samples were photoexcited with a pump fluence of 2.0 μJ cm^{-2} at 400 nm which is generated using a BBO crystal, and the TRPL signals were collected in a conventional backscattering geometry through a microscope objective. Emission light was then dispersed by a DK240 1/4 m monochromator with 300 g mm^{-1} grating and collected by an Optronis Optoscope streak camera which has an ultimate temporal resolution of ~6 ps when operating with the fastest synchroscan parameters. Microscopic steady-state absorption and scattering spectra were recorded with a homemade confocal microscope system with the spatial resolution ~1 μm.[59−62]

FDTD Calculation. A commercially available FDTD simulation software package, Lumerical, was used to perform the Full-field electromagnetic wave calculations. Given the quasi-one dimension characteristics of Ag NW, two-dimensional simulation scenario was used as the NW direction can be treated to be infinite long. Antisymmetric boundary condition was set along the polarization of electromagnetic waves (x axis); perfectly matched layers were used along the propagation of electromagnetic waves (y axis). The simulation pitch used is 1000 nm × 1500 nm in the x- and y-directions, respectively. Electric and magnetic fields are detected using frequency profile monitors. Dielectric constants of P3HT:PCBM, ITO, PEDOT:PSS and Ag are extracted from other reports.[63−65]

Conflict of Interest: The authors declare no competing financial interest.

Acknowledgment. T.C.S. acknowledges the support from the following research grants: NTU start-up grants (M4080514); SPMS collaborative Research Award (M4080536); Ministry of Education (MOE) Academic Research Fund (AcRF) Tier 2 grant MOE2013-T2-1-081; and the Competitive Research Programme (CRP) grant under Project No. NRF-CRP5-2009-04. N.M. acknowledges the support from his NTU start-up grant (M4081293). Q.X. acknowledges the support of this work from the Singapore National Research Foundation (NRF) through NRF fellowship grant (NRF-RF2009-06) and a Competitive Research Program grant (NRF-CRP-6-2010-2), Ministry of Education AcRF Tier 2 Grant (MOE2011-T2-2-051), and start-up grant support (M58113004) from Nanyang Technological University (NTU). Q.X., N.M., and T.C.S. also acknowledge the financial support by the Singapore NRF through the Singapore-Berkeley Research Initiative for Sustainable Energy (SinBeRISE) CREATE Programme.

Supporting Information Available: AFM image of a single Ag NW coated with PEDOT:PSS layer and of Ag NW after coating with active layer (P3HT:PCBM); scheme of home-made micro-area measurement setup; FDTD simulation results of the absorption and scattering spectra of single silver nanowires; electric field distribution from a single Ag nanowire on quartz following excitation by 0° polarization light from the z-direction; scheme for the micro-transient absorption spectroscopy setup; micro-area $I-V$ curves for different single nanowire doped OPV devices; table of previous literature reports on the efficiency enhancement in plasmonic organic solar cells. This material is available free of charge *via* the Internet at http://pubs.acs.org.

REFERENCES AND NOTES

1. Yu, G.; Gao, J.; Hummelen, J. C.; Wudl, F.; Heeger, A. J. Polymer Photovoltaic Cells-Enhanced Efficiencies *via* a Network of Internal Donor-Acceptor Heterojunctins. *Science* **1995**, *270*, 1789–1791.
2. Gunes, S.; Neugebauer, H.; Sariciftci, N. S. Conjugated Polymer-Based Organic Solar Cells. *Chem. Rev. (Washington, DC, U.S.)* **2007**, *107*, 1324–1338.
3. Thompson, B. C.; Fréchet, J. M. J. Polymer–Fullerene Composite Solar Cells. *Angew. Chem., Int. Ed.* **2008**, *47*, 58–77.
4. Wang, D. H.; Moon, J. S.; Seifter, J.; Jo, J.; Park, J. H.; Park, O. O.; Heeger, A. J. Sequential Processing: Control of Nanomorphology in Bulk Heterojunction Solar Cells. *Nano Lett.* **2011**, *11*, 3163–3168.
5. Hoth, C. N.; Schilinsky, P.; Choulis, S. A.; Brabec, C. J. Printing Highly Efficient Organic Solar Cells. *Nano Lett.* **2008**, *8*, 2806–2813.
6. Service, R. F. Outlook Brightens for Plastic Solar Cells. *Science* **2011**, *332*, 293–293.
7. Green, M. A.; Emery, K.; Hishikawa, Y.; Warta, W.; Dunlop, E. D. Solar Cell Efficiency Tables (Version 43). *Prog. Photovoltaics* **2014**, *22*, 1–9.
8. Choi, H.; Lee, J.-P.; Ko, S.-J.; Jung, J.-W.; Park, H.; Yoo, S.; Park, O.; Jeong, J.-R.; Park, S.; Kim, J. Y. Multipositional Silica-Coated Silver Nanoparticles for High-Performance Polymer Solar Cells. *Nano Lett.* **2013**, *13*, 2204–2208.
9. Wang, D. H.; Park, K. H.; Seo, J. H.; Seifter, J.; Jeon, J. H.; Kim, J. K.; Park, J. H.; Park, O. O.; Heeger, A. J. Enhanced Power Conversion Efficiency in PCDTBT/PC70BM Bulk Heterojunction Photovoltaic Devices with Embedded Silver Nanoparticle Clusters. *Adv. Energy Mater.* **2011**, *1*, 766–770.
10. Baek, S.-W.; Park, G.; Noh, J.; Cho, C.; Lee, C.-H.; Seo, M.-K.; Song, H.; Lee, J.-Y. Au@Ag Core–Shell Nanocubes for Efficient Plasmonic Light Scattering Effect in Low Bandgap Organic Solar Cells. *ACS Nano* **2014**, *8*, 3302–3312.
11. Jung, K.; Song, H.-J.; Lee, G.; Ko, Y.; Ahn, K.; Choi, H.; Kim, J. Y.; Ha, K.; Song, J.; Lee, J.-K.; *et al.* Plasmonic Organic Solar Cells Employing Nanobump Assembly *via* Aerosol-Derived Nanoparticles. *ACS Nano* **2014**, *8*, 2590–2601.
12. Lu, L.; Xu, T.; Chen, W.; Lee, J. M.; Luo, Z.; Jung, I. H.; Park, H. I.; Kim, S. O.; Yu, L. The Role of N-Doped Multiwall Carbon Nanotubes in Achieving Highly Efficient Polymer Bulk Heterojunction Solar Cells. *Nano Lett.* **2013**, *13*, 2365–2369.
13. Yang, J.; You, J.; Chen, C.-C.; Hsu, W.-C.; Tan, H.-r.; Zhang, X. W.; Hong, Z.; Yang, Y. Plasmonic Polymer Tandem Solar Cell. *ACS Nano* **2011**, *5*, 6210–6217.
14. Paz-Soldan, D.; Lee, A.; Thon, S. M.; Adachi, M. M.; Dong, H.; Maraghechi, P.; Yuan, M.; Labelle, A. J.; Hoogland, S.; Liu, K.; *et al.* Jointly Tuned Plasmonic–Excitonic Photovoltaics Using Nanoshells. *Nano Lett.* **2013**, *13*, 1502–1508.
15. Atwater, H. A.; Polman, A. Plasmonics for Improved Photovoltaic Devices. *Nat. Mater.* **2010**, *9*, 205–213.
16. Lu, L.; Luo, Z.; Xu, T.; Yu, L. Cooperative Plasmonic Effect of Ag and Au Nanoparticles on Enhancing Performance of Polymer Solar Cells. *Nano Lett.* **2012**, *13*, 59–64.
17. Lunz, M.; Zhang, X.; Gerard, V. A.; Gun'ko, Y. K.; Lesnyak, V.; Gaponik, N.; Susha, A. S.; Rogach, A. L.; Bradley, A. L. Effect of Metal Nanoparticle Concentration on Localized Surface Plasmon Mediated Forster Resonant Energy Transfer. *J. Phys. Chem. C* **2012**, *116*, 26529–26534.
18. Kim, C. H.; Cha, S. H.; Kim, S. C.; Song, M.; Lee, J.; Shin, W. S.; Moon, S. J.; Bahng, J. H.; Kotov, N. A.; Jin, S. H. Silver Nanowire Embedded in P3HT: PCBM for High-Efficiency Hybrid Photovoltaic Device Applications. *ACS Nano* **2011**, *5*, 3319–3325.
19. Xue, M.; Li, L.; de Villers, B. J. T.; Shen, H. J.; Zhu, J. F.; Yu, Z. B.; Stieg, A. Z.; Pei, Q. B.; Schwartz, B. J.; Wang, K. L. Charge-Carrier Dynamics in Hybrid Plasmonic Organic Solar Cells with Ag Nanoparticles. *Appl. Phys. Lett.* **2011**, *98*, 253302–253304.
20. Topp, K.; Borchert, H.; Johnen, F.; Tune, A. V.; Knipper, M.; von Hauff, E.; Parisi, J.; Al-Shamery, K. Impact of the Incorporation of Au Nanoparticles into Polymer/Fullerene Solar Cells. *J. Phys. Chem. A* **2010**, *114*, 3981–3989.
21. Wu, B.; Oo, T. Z.; Li, X. L.; Liu, X. F.; Wu, X. Y.; Yeow, E. K. L.; Fan, H. J.; Mathews, N.; Sum, T. C. Efficiency Enhancement in Bulk-Heterojunction Solar Cells Integrated with Large-Area Ag Nanotriangle Arrays. *J. Phys. Chem. C* **2012**, *116*, 14820–14825.
22. Kim, K.; Carroll, D. L. Roles of Au and Ag Nanoparticles in Efficiency Enhancement of Poly(3-octylthiophene)/C60 Bulk Heterojunction Photovoltaic Devices. *Appl. Phys. Lett.* **2005**, *87*, 203113–203115.
23. Morfa, A. J.; Rowlen, K. L.; Reilly, T. H.; Romero, M. J.; van de Lagemaat, J. Plasmon-Enhanced Solar Energy Conversion in Organic Bulk Heterojunction Photovoltaics. *Appl. Phys. Lett.* **2008**, *92*, 013504–013506.

24. Oo, T. Z.; Mathews, N.; Xing, G. C.; Wu, B.; Xing, B. G.; Wong, L. H.; Sum, T. C.; Mhaisalkar, S. G. Ultrafine Gold Nanowire Networks as Plasmonic Antennae in Organic Photovoltaics. *J. Phys. Chem. C* **2012**, *116*, 6453–6458.
25. Paci, B.; Spyropoulos, G. D.; Generosi, A.; Bailo, D.; Albertini, V. R.; Stratakis, E.; Kymakis, E. Enhanced Structural Stability and Performance Durability of Bulk Heterojunction Photovoltaic Devices Incorporating Metallic Nanoparticles. *Adv. Funct. Mater.* **2011**, *21*, 3573–3582.
26. Fung, D. D. S.; Qiao, L.; Choy, W. C. H.; Wang, C.; Sha, W. E. I.; Xie, F.; He, S. Optical and Electrical Properties of Efficiency Enhanced Polymer Solar Cells with Au Nanoparticles in a PEDOT-PSS Layer. *J. Mater. Chem.* **2011**, *21*, 16349–16356.
27. Li, X.; Choy, W. C. H.; Lu, H.; Sha, W. E. I.; Ho, A. H. P. Efficiency Enhancement of Organic Solar Cells by Using Shape-Dependent Broadband Plasmonic Absorption in Metallic Nanoparticles. *Adv. Funct. Mater.* **2013**, *23*, 2728–2735.
28. Kulkarni, A. P.; Noone, K. M.; Munechika, K.; Guyer, S. R.; Ginger, D. S. Plasmon-Enhanced Charge Carrier Generation in Organic Photovoltaic Films Using Silver Nanoprisms. *Nano Lett.* **2010**, *10*, 1501–1505.
29. Baek, S.-W.; Noh, J.; Lee, C.-H.; Kim, B.; Seo, M.-K.; Lee, J.-Y. Plasmonic Forward Scattering Effect in Organic Solar Cells: A Powerful Optical Engineering Method. *Sci. Rep.* **2013**, *3*, 1726.
30. Fu, W.-F.; Chen, X.; Yang, X.; Wang, L.; Shi, Y.; Shi, M.; Li, H.-Y.; Jen, A. K. Y.; Chen, J.-W.; Cao, Y.; *et al.* Optical and Electrical Effects of Plasmonic Nanoparticles in High-Efficiency Hybrid Solar Cells. *Phys. Chem. Chem. Phys.* **2013**, *15*, 17105–17111.
31. Hsiao, Y.-S.; Charan, S.; Wu, F.-Y.; Chien, F.-C.; Chu, C.-W.; Chen, P.; Chen, F.-C. Improving the Light Trapping Efficiency of Plasmonic Polymer Solar Cells through Photon Management. *J. Phys. Chem. C* **2012**, *116*, 20731–20737.
32. Chen, F.-C.; Wu, J.-L.; Lee, C.-L.; Hong, Y.; Kuo, C.-H.; Huang, M. H. Plasmonic-Enhanced Polymer Photovoltaic Devices Incorporating Solution-Processable Metal Nanoparticles. *Appl. Phys. Lett.* **2009**, *95*, 013305.
33. Chuang, M.-K.; Lin, S.-W.; Chen, F.-C.; Chu, C.-W.; Hsu, C.-S. Gold Nanoparticle-Decorated Graphene Oxides for Plasmonic-Enhanced Polymer Photovoltaic Devices. *Nanoscale* **2014**, *6*, 1573–1579.
34. Wu, B.; Wu, X.; Guan, C.; Fai Tai, K.; Yeow, E. K. L.; Jin Fan, H.; Mathews, N.; Sum, T. C. Uncovering Loss Mechanisms in Silver Nanoparticle-Blended Plasmonic Organic Solar Cells. *Nat. Commun.* **2013**, *4*, 2004.
35. Lee, J.-Y.; Connor, S. T.; Cui, Y.; Peumans, P. Solution-Processed Metal Nanowire Mesh Transparent Electrodes. *Nano Lett.* **2008**, *8*, 689–692.
36. Lee, M.-S.; Lee, K.; Kim, S.-Y.; Lee, H.; Park, J.; Choi, K.-H.; Kim, H.-K.; Kim, D.-G.; Lee, D.-Y.; Nam, S.; *et al.* High-Performance, Transparent, and Stretchable Electrodes Using Graphene–Metal Nanowire Hybrid Structures. *Nano Lett.* **2013**, *13*, 2814–2821.
37. Lee, J.-Y.; Connor, S. T.; Cui, Y.; Peumans, P. Semitransparent Organic Photovoltaic Cells with Laminated Top Electrode. *Nano Lett.* **2010**, *10*, 1276–1279.
38. Hu, L.; Kim, H. S.; Lee, J.-Y.; Peumans, P.; Cui, Y. Scalable Coating and Properties of Transparent, Flexible, Silver Nanowire Electrodes. *ACS Nano* **2010**, *4*, 2955–2963.
39. Halas, N. J. Plasmonics: An Emerging Field Fostered by Nano Letters. *Nano Lett.* **2010**, *10*, 3816–3822.
40. Gan, Q.; Bartoli, F. J.; Kafafi, Z. H. Plasmonic-Enhanced Organic Photovoltaics: Breaking the 10% Efficiency Barrier. *Adv. Mater. (Weinheim, Ger.)* **2013**, *25*, 2385–2396.
41. Handloser, M.; Dunbar, R. B.; Wisnet, A.; Altpeter, P.; Scheu, C.; Schmidt-Mende, L.; Hartschuh, A. Influence of Metallic and Dielectric Nanowire Arrays on the Photoluminescence Properties of P3HT Thin Films. *Nanotechnology* **2012**, *23*, 305402.
42. Tao, A.; Kim, F.; Hess, C.; Goldberger, J.; He, R.; Sun, Y.; Xia, Y.; Yang, P. Langmuir–Blodgett Silver Nanowire Monolayers for Molecular Sensing Using Surface-Enhanced Raman Spectroscopy. *Nano Lett.* **2003**, *3*, 1229–1233.
43. Al-Rawashdeh, N. A. F.; Sandrock, M. L.; Seugling, C. J.; Foss, C. A. Visible Region Polarization Spectroscopic Studies of Template-Synthesized Gold Nanoparticles Oriented in Polyethylene. *J. Phys. Chem. B* **1998**, *102*, 361–371.
44. Lassiter, J. B.; Knight, M. W.; Mirin, N. A.; Halas, N. J. Reshaping the Plasmonic Properties of an Individual Nanoparticle. *Nano Lett.* **2009**, *9*, 4326–4332.
45. Wiley, B.; Sun, Y.; Xia, Y. Synthesis of Silver Nanostructures with Controlled Shapes and Properties. *Acc. Chem. Res.* **2007**, *40*, 1067–1076.
46. Yakimov, A.; Forrest, S. R. High Photovoltage Multiple-Heterojunction Organic Solar Cells Incorporating Interfacial Metallic Nanoclusters. *Appl. Phys. Lett.* **2002**, *80*, 1667–1669.
47. Munechika, K.; Chen, Y.; Tillack, A. F.; Kulkarni, A. P.; Plante, I. J.-L.; Munro, A. M.; Ginger, D. S. Spectral Control of Plasmonic Emission Enhancement from Quantum Dots near Single Silver Nanoprisms. *Nano Lett.* **2010**, *10*, 2598–2603.
48. Wu, J.-L.; Chen, F.-C.; Hsiao, Y.-S.; Chien, F.-C.; Chen, P.; Kuo, C.-H.; Huang, M. H.; Hsu, C.-S. Surface Plasmonic Effects of Metallic Nanoparticles on the Performance of Polymer Bulk Heterojunction Solar Cells. *ACS Nano* **2011**, *5*, 959–967.
49. Piris, J.; Dykstra, T. E.; Bakulin, A. A.; Loosdrecht, P. H. M. v.; Knulst, W.; Trinh, M. T.; Schins, J. M.; Siebbeles, L. D. A. Photogeneration and Ultrafast Dynamics of Excitons and Charges in P3HT/PCBM Blends. *J. Phys. Chem. C* **2009**, *113*, 14500–14506.
50. Guo, J.; Ohkita, H.; Benten, H.; Ito, S. Near-IR Femtosecond Transient Absorption Spectroscopy of Ultrafast Polaron and Triplet Exciton Formation in Polythiophene Films with Different Regioregularities. *J. Am. Chem. Soc.* **2009**, *131*, 16869–16880.
51. Guo, J.; Ohkita, H.; Benten, H.; Ito, S. Charge Generation and Recombination Dynamics in Poly(3-hexylthiophene)/Fullerene Blend Films with Different Regioregularities and Morphologies. *J. Am. Chem. Soc.* **2010**, *132*, 6154–6164.
52. Shuttle, C. G.; O'Regan, B.; Ballantyne, A. M.; Nelson, J.; Bradley, D. D. C.; Durrant, J. R. Bimolecular Recombination Losses in Polythiophene: Fullerene Solar Cells. *Phys. Rev. B* **2008**, *78*, 113201.
53. Xie, F. X.; Choy, W. C. H.; Wang, C. C. D.; Sha, W. E. I.; Fung, D. D. S. Improving the Efficiency of Polymer Solar Cells by Incorporating Gold Nanoparticles into All Polymer Layers. *Appl. Phys. Lett.* **2011**, *99*, 153304–153306.
54. Nehl, C. L.; Grady, N. K.; Goodrich, G. P.; Tam, F.; Halas, N. J.; Hafner, J. H. Scattering Spectra of Single Gold Nanoshells. *Nano Lett.* **2004**, *4*, 2355–2359.
55. Zhang, Y.; Barhoumi, A.; Lassiter, J. B.; Halas, N. J. Orientation-Preserving Transfer and Directional Light Scattering from Individual Light-Bending Nanoparticles. *Nano Lett.* **2011**, *11*, 1838–1844.
56. Link, S.; El-Sayed, M. A. Shape and Size Dependence of Radiative, Non-Radiative and Photothermal Properties of Gold Nanocrystals. *Int. Rev. Phys. Chem.* **2000**, *19*, 409–453.
57. Xia, Y.; Yang, P.; Sun, Y.; Wu, Y.; Mayers, B.; Gates, B.; Yin, Y.; Kim, F.; Yan, H. One-Dimensional Nanostructures: Synthesis, Characterization, and Applications. *Adv. Mater. (Weinheim, Ger.)* **2003**, *15*, 353–389.
58. Zhang, Q.; Shan, X. Y.; Zhou, L.; Zhan, T. R.; Wang, C. X.; Li, M.; Jia, J. F.; Zi, J.; Wang, Q. Q.; Xue, Q. K. Scattering Focusing and Localized Surface Plasmons in a Single Ag Nanoring. *Appl. Phys. Lett.* **2010**, *97*, 261107.
59. Liu, X.; Zhang, Q.; Xiong, Q.; Sum, T. C. Tailoring the Lasing Modes in Semiconductor Nanowire Cavities Using Intrinsic Self-Absorption. *Nano Lett.* **2013**, *13*, 1080–1085.
60. Liu, X.; Zhang, Q.; Yip, J. N.; Xiong, Q.; Sum, T. C. Wavelength Tunable Single Nanowire Lasers Based on Surface Plasmon Polariton Enhanced Burstein–Moss Effect. *Nano Lett.* **2013**, *13*, 5336–5343.
61. Liu, X.; Zhang, Q.; Xing, G.; Xiong, Q.; Sum, T. C. Size-Dependent Exciton Recombination Dynamics in Single CdS Nanowires beyond the Quantum Confinement Regime. *J. Phys. Chem. C* **2013**, *117*, 10716–10722.

62. Zhang, Q.; Liu, X.; Utama, M. I. B.; Zhang, J.; de la Mata, M.; Arbiol, J.; Lu, Y.; Sum, T. C.; Xiong, Q. Highly Enhanced Exciton Recombination Rate by Strong Electron−Phonon Coupling in Single ZnTe Nanobelt. *Nano Lett.* **2012**, *12*, 6420–6427.
63. Schmidt-Mende, L.; Watson, M.; Müllen, K.; Friend, R. H. Organic Thin Film Photovoltaic Devices from Discotic Materials. *Mol. Cryst. Liq. Cryst.* **2003**, *396*, 73–90.
64. Dennler, G.; Forberich, K.; Ameri, T.; Waldauf, C.; Denk, P.; Brabec, C. J.; Hingerl, K.; Heeger, A. J. Design of Efficient Organic Tandem Cells: On the Interplay Between Molecular Absorption and Layer Sequence. *J. Appl. Phys.* **2007**, *102*, 123109.
65. Monestier, F.; Simon, J. J.; Torchio, P.; Escoubas, L.; Florya, F.; Bailly, S.; de Bettignies, R.; Guillerez, S.; Defranoux, C. Modeling the Short-Circuit Current Censity of Polymer Solar Cells Based on P3HT: PCBM Blend. *Sol. Energy Mater. Sol. Cells* **2007**, *91*, 405–410.